

<sup>1</sup> A novel inf–sup–based volumetric constraint ratio and  
<sup>2</sup> its implementation via mixed FE-meshfree formulation

<sup>3</sup> Junchao Wu<sup>a,\*</sup>, Yingjie Chu<sup>b</sup>, Yangtao Xu<sup>a</sup>

<sup>a</sup> Key Laboratory for Intelligent Infrastructure and Monitoring of Fujian Province, College  
of Civil Engineering, Huaqiao University , Xiamen, Fujian, 361021, China

<sup>b</sup> Fujian Key Laboratory of Digital Simulations for Coastal Civil Engineering, Department  
of Civil Engineering, Xiamen University , Xiamen, Fujian, 361005, China

---

<sup>4</sup> **Abstract**

Numerical formulations for incompressible materials often suffer from volumetric locking, which reduces the accuracy of displacement solutions and introduces oscillations in the pressure field. A well-chosen constraint ratio can mitigate this issue, but traditional approaches lack a theoretical foundation based on the inf–sup (or LBB) condition, which is essential for the stability of mixed formulations. This paper introduces a novel optimal constraint ratio derived from the inf–sup condition to address volumetric locking. The inf–sup test, a numerical tool for verifying the inf–sup condition, is reaffirmed to be equivalent to the inf–sup condition through a variational approach. By incorporating a complete polynomial space whose dimension matches the number of displacement degrees of freedom (DOFs), a new inf–sup value estimator is developed, explicitly considering the constraint ratio. For a given number of displacement DOFs, when the pressure DOFs of a numerical formulation remain below a stabilized number that falls into the optimal constraint ratio range, this numerical formulation actually satisfies the inf–sup condition. To implement the optimal constraint ratio, a mixed finite element and meshfree formulation is proposed, where displacements are discretized using traditional finite element approximations, and pressures are approximated via the reproducing kernel meshfree method. Leveraging the globally smooth reproducing kernel shape functions, the constraint ratio can be flexibly adjusted to meet the inf–sup condition without the limit of element. For computational efficiency and ease of implementation, pressure nodes are placed on selected displacement nodes to maintain the optimal constraint ratio. Inf–sup tests and a series of 2D and 3D incompressible elasticity examples validate the proposed constraint ratio, demonstrating its effectiveness in eliminating volumetric locking and enhancing the performance of mixed finite element and meshfree formulations.

<sup>5</sup> **Keywords:** Optimal constraint ratio, Inf–sup condition estimator, Volumetric  
<sup>6</sup> locking, Mixed formulation, Reproducing kernel meshfree approximation

---

---

\*Corresponding author

Email address: [jcwu@hqu.edu.cn](mailto:jcwu@hqu.edu.cn) (Junchao Wu)

7      **1. Introduction**

8      The volumetric constraint is a necessary condition in the numerical formulation  
 9      of incompressible materials like rubber and hydrogel. Proper imposition of  
 10     this constraint is crucial for obtaining better numerical solutions; insufficient or  
 11     excessive constraints will reduce the accuracy and stability of the solution [1].  
 12     The volumetric constraint ratio [2], denoted as  $r$ , is often used to measure the  
 13     level of constraint. It is defined as the total degrees of freedom (DOFs) of dis-  
 14     placement divided by the total DOFs of pressure. Ideally, the optimal constraint  
 15     ratio should be consistent with its governing partial differential equations. For  
 16     example, in the two-dimensional (2D) case, the optimal constraint ratio is 2,  
 17     since there are two governing equations for displacement and one for pressure.  
 18     When the constraint ratio is less than 2, the formulation suffers from volumetric  
 19     locking, while a constraint ratio greater than 2 can cause a coarse solution for  
 20     pressure. These observations have been summarized as follows[2]:

$$r = \frac{2n_u}{n_p}, \quad \begin{cases} r > 2 & \text{too few constraints} \\ r = 2 & \text{optimal} \\ r < 2 & \text{too many constraints} \\ r \leq 1 & \text{severe locking} \end{cases} \quad (1)$$

21     where  $n_u$  and  $n_p$  are the numbers of control nodes for displacement and pressure,  
 22     respectively. Classifying the locked status via the constraint ratio is straight-  
 23     forward but imprecise. For instance, the constraint ratio can remain 2 while  
 24     the pressure is discretized using continuous shape functions identical to the  
 25     displacement's approximation. However, volumetric locking still exists in this  
 26     formulation [2].

27     The inf-sup condition, also known as the Ladyzhenskay–Babuka–Brezzi  
 28     (LBB) condition [3, 4], is a more precise requirement for a locking-free for-  
 29     mulation. This condition is based on the mixed formulation framework, and  
 30     when the inf-sup condition is satisfied, both the accuracy and stability of the  
 31     mixed-formulation can be ensured. However, verifying the inf-sup condition is  
 32     non-trivial. An eigenvalue problem namely inf-sup test can be used to check  
 33     this condition numerically [5, 6, 7, 8]. Analytically, Brezzi and Fortin proposed  
 34     a two-level projection framework that always satisfies the inf-sup condition, al-  
 35     lowing it to be checked by identifying whether the formulation is included in  
 36     this framework. Both analytical and numerical methods to check the inf-sup  
 37     condition are complex, and the relationship between the constraint ratio and  
 38     the inf-sup condition remains unclear.

39     To address volumetric constraint issues, adjusting the constraint ratio to an  
 40     appropriate level is commonly used and easily implemented. In traditional finite  
 41     element methods (FEM), this adjustment is carried out based on elements since  
 42     the DOFs are embedded in each element. Conventional FEM often exhibits  
 43     an over-constrained status. Reducing the approximation order of pressure in  
 44     mixed formulation can alleviate the constraint burden, such as with the well-  
 45     known Q4P1 (4-node quadrilateral displacement element with 1-node piecewise

constant pressure element) and Q8P3. Globally, using continuous shape functions to link the local pressure DOFs in each element can also reduce the total number of pressure DOFs and increase the constraint ratio, such as with T6C3 (6-node triangular displacement element with 3-node continuous linear pressure element) and Q9C4 (Taylor–Hood element) [9]. These schemes belong to the mixed formulation framework and can also be implemented through a projection approach, where the pressure approximant is projected into a lower-dimensional space. Examples include selective integration methods [10, 11], B–bar or F–bar methods [12, 13, 14, 15], pressure projection methods [16, 17, 18, 19, 20], and enhanced strain method [21]. Meanwhile, conventional 3-node triangular elements arranged in a regular cross pattern can also reduce the dimension of the pressure space [22]. It should be noted that not all of these methods meet the inf–sup condition despite alleviating volumetric locking and producing a good displacement solution. Some methods, like Q4P1, show significant oscillation for the pressure solution, known as spurious pressure mode or checkerboard mode [22]. In such cases, additional stabilization approaches, such as variational multi-scale stabilization (VMS) [23, 24, 25, 26, 27], Galerkin/least-squares (GLS) [28], or Streamline upwind/Petrov–Galerkin formulation (SUPG) [29, 30] are required to eliminate the oscillations in pressure.

Another class of FEM methods adjusts the constraint ratio by increasing the displacement DOFs. For instance, based on 3-node triangular elements, Arnold et al. [31, 32] used a cubic bubble function in each element to increase the displacement DOFs, known as the MINI element. It has been shown that this method belongs to the VMS framework [33], and its fulfillment of the inf–sup condition can be analytically evidenced using the two-level projection framework [7]. The Crouzeix–Raviart element [34] transfers the DOFs from the triangular vertices to edges, increasing the constraint ratio since, for triangular topology, the number of edges is greater than that of vertices. More details about FEM technology for volumetric constraint issues can be found in Refs. [2, 4, 35].

In the past two decades, various novel approximations equipped with globally smooth shape functions, such as moving least-squares approximation [36], reproducing kernel approximation [37, 38], radial basis functions [39, 40], maximum-entropy approximation [41], and NURBS approximation [42, 43], have been proposed. In these approaches, the approximant pressure evaluated by the derivatives of globally continuous shape functions also maintains a constraint ratio of 2 in 2D incompressible elasticity problems. However, the corresponding results still show lower accuracy caused by locking [44, 45]. Widely-used locking-free technologies for FEM are introduced in these approaches to enhance their performance. For example, Moutsanidis et al. [46, 47] employed selective integration and B–bar, F–bar methods for reproducing kernel particle methods. Wang et al. [48] applied selective integration schemes with bubble-stabilized functions to node-based smoothed particle FEM. Elguedj et al. [49] proposed the B–bar and F–bar NURBS formulations for linear and nonlinear incompressible elasticity. Chen et al. [50] adopted the pressure projection approach for reproducing kernel formulations for nearly-incompressible problems, which was later extended

to Stokes flow formulations by Goh et al. [51]. Bombarde et al. [52] developed a block-wise NURBS formulation for shell structures, eliminating locking via pressure projection. Casquero and Golestanian [53] proposed a NURBS-based continuous-assumed-strain element to alleviate volumetric locking. Most of these approximations offer better flexibility for arranging DOFs since their shape function constructions are no longer element-dependent. Huerta et al.[54] proposed a reproducing kernel approximation with divergence-free basis functions to avoid volumetric strain entirely , although this approach is unsuitable for compressible cases. Wu et al. [55] added extra displacement DOFs in FEM elements to resolve the locking issue, constructing local shape functions using generalized meshfree interpolation to maintain consistency. Vu-Huu et al. [56] employed different-order polygonal finite element shape functions to approximate displacement and pressure, embedding a bubble function in each element for stabilization.

This work proposes a more precise optimal volumetric constraint ratio and implements a locking-free mixed FE-meshfree formulation with this optimal constraint ratio. Firstly, the inf-sup condition is derived in a new form, showing that the inf-sup value equals to the lowest non-zero eigenvalue of dilatation stiffness in the context of variational analysis. Subsequently, involving a complete polynomial space with dimensions identical to displacement DOFs, the number of non-zero eigenvalues can be analytically calculated, and a new estimator considering the constraint ratio is established. From this estimator, the optimal constraint ratio is defined with a stabilized number of pressure nodes. If the constraint ratio exceeds the locking ratio, the formulation will show severe locking. When the constraint ratio is lower than the optimal ratio, the formulation achieves satisfactory results, and the inf-sup condition is fulfilled. This estimator provides a strong link between the inf-sup value and the pressure DOFs, making it possible to justify the locking status by counting the pressure nodes. Furthermore, a mixed FE-meshfree formulation is proposed to verify the optimal constraint ratio. In this mixed formulation, the displacement is approximated by traditional finite element methods, and the pressure is discretized by reproducing kernel meshfree approximation. With the aid of global RK shape functions, the pressure's DOFs can be adjusted arbitrarily without considering approximation order and numerical integration issues to maintaining the constraint ratio as optimal.

The remainder of this paper is organized as follows: Section 2 reviews the mixed formulation framework for incompressible elasticity problems. In Section 3, a novel estimator of the inf-sup value is developed, from which the optimal constraint ratio is obtained. Section 4 introduces the mixed FE-meshfree formulation and its corresponding nodal distribution schemes. Section 5 verifies the proposed optimal constraint ratio using a set of benchmark incompressible elasticity examples, studying error convergence and stability property for the mixed FE-meshfree approximation. Finally, the conclusions are presented in Section 6.

<sup>136</sup> **2. Mixed-formulation**

<sup>137</sup> *2.1. Nearly-incompressible elasticity*

<sup>138</sup> Consider a body  $\Omega \in \mathbb{R}^{n_d}$  with boundary  $\Gamma$  in  $n_d$ -dimension, where  $\Gamma_t$  and  
<sup>139</sup>  $\Gamma_g$  denote its natural boundary and essential boundary, respectively, such that  
<sup>140</sup>  $\Gamma_t \cup \Gamma_g = \Gamma$ ,  $\Gamma_t \cap \Gamma_g = \emptyset$ . The corresponding governing equations for the mixed  
<sup>141</sup> formulation are given by:

$$\begin{cases} \nabla \cdot \boldsymbol{\sigma} + \mathbf{b} = \mathbf{0} & \text{in } \Omega \\ \frac{p}{\kappa} + \nabla \cdot \mathbf{u} = 0 & \text{in } \Omega \\ \boldsymbol{\sigma} \cdot \mathbf{n} = \mathbf{t} & \text{on } \Gamma_t \\ \mathbf{u} = \mathbf{g} & \text{on } \Gamma_g \end{cases} \quad (2)$$

<sup>142</sup> where  $\mathbf{b}$  denotes the prescribed body force in  $\Omega$ .  $\mathbf{t}, \mathbf{g}$  are prescribed traction and  
<sup>143</sup> displacement on natural and essential boundaries, respectively.  $\mathbf{u}$  and  $p$ , standing  
<sup>144</sup> for displacement and hydrostatic pressure, respectively, are the variables of  
<sup>145</sup> this problem.  $\nabla$  is the gradient tensor defined by  $\nabla = \frac{\partial}{\partial x_i} \mathbf{e}_i$ .  $\boldsymbol{\sigma}$  denotes the  
<sup>146</sup> stress tensor and has the following form:

$$\boldsymbol{\sigma}(\mathbf{u}, p) = p \mathbf{1} + 2\mu \nabla^d \mathbf{u} \quad (3)$$

<sup>147</sup> in which  $\mathbf{1} = \delta_{ij} \mathbf{e}_i \otimes \mathbf{e}_j$  is the second-order identity tensor.  $\nabla^d \mathbf{u}$  is the deviatoric  
<sup>148</sup> gradient of  $\mathbf{u}$  and can be evaluated by:

$$\nabla^d \mathbf{u} = \frac{1}{2} (\mathbf{u} \nabla + \nabla \mathbf{u}) - \left( \frac{1}{3} \nabla \cdot \mathbf{u} \right) \mathbf{1} \quad (4)$$

<sup>149</sup> and  $\kappa, \mu$  are the bulk modulus and shear modulus, respectively, and they can  
<sup>150</sup> be represented by Young's modulus  $E$  and Poisson's ratio  $\nu$ :

$$\kappa = \frac{E}{2(1-2\nu)}, \quad \mu = \frac{E}{3(1+\nu)} \quad (5)$$

<sup>151</sup> In accordance with the Galerkin formulation, the weak form can be given  
<sup>152</sup> by: Find  $\mathbf{u} \in V, p \in Q$ , such that

$$\begin{cases} a(\mathbf{v}, \mathbf{u}) + b(\mathbf{v}, p) = f(\mathbf{v}) & \forall \mathbf{v} \in V \\ b(\mathbf{u}, q) + c(q, p) = 0 & \forall q \in Q \end{cases} \quad (6)$$

<sup>153</sup> with the spaces  $V, Q$  defined by:

$$V = \{\mathbf{v} \in H^1(\Omega)^2 \mid \mathbf{v} = \mathbf{g}, \text{ on } \Gamma_g\} \quad (7)$$

$$Q = \{q \in L^2(\Omega) \mid \int_{\Omega} q d\Omega = 0\} \quad (8)$$

<sup>154</sup> where  $a : V \times V \rightarrow \mathbb{R}$ ,  $b : V \times Q \rightarrow \mathbb{R}$  and  $c : Q \times Q \rightarrow \mathbb{R}$  are bilinear forms,  
<sup>155</sup> and  $f : V \rightarrow \mathbb{R}$  is the linear form. In elasticity problems, they are given by:

$$a(\mathbf{v}, \mathbf{u}) = \int_{\Omega} \nabla^d \mathbf{v} : \nabla^d \mathbf{u} d\Omega \quad (9)$$

$$b(\mathbf{v}, q) = \int_{\Omega} \nabla \cdot \mathbf{v} q d\Omega \quad (10)$$

$$c(q, p) = - \int_{\Omega} \frac{1}{3\kappa} q p d\Omega \quad (11)$$

$$f(\mathbf{v}) = \int_{\Gamma_t} \mathbf{v} \cdot \mathbf{t} d\Gamma + \int_{\Omega} \mathbf{v} \cdot \mathbf{b} d\Omega \quad (12)$$

<sup>156</sup> 2.2. Ritz–Galerkin problem and volumetric locking

<sup>157</sup> In the mixed-formulation framework, the displacement and pressure can be  
<sup>158</sup> discretized by different approximations. The approximant displacement  $\mathbf{u}_h$  and  
<sup>159</sup> approximant pressure  $p_h$  can be expressed by:

$$\mathbf{u}_h(\mathbf{x}) = \sum_{I=1}^{n_u} N_I(\mathbf{x}) \mathbf{u}_I, \quad p_h(\mathbf{x}) = \sum_{K=1}^{n_p} \Psi_K(\mathbf{x}) p_K \quad (13)$$

<sup>160</sup> where  $N_I$  and  $\Psi_K$  are the shape functions for the displacement and pressure,  $\mathbf{u}_I$   
<sup>161</sup> and  $p_K$  are the corresponding coefficients. Leading these approximations into  
<sup>162</sup> the weak form of Eq. (6) yields the following Ritz–Galerkin problems: Find  
<sup>163</sup>  $\mathbf{u}_h \in V_h$ ,  $p_h \in Q_h$ , such that

$$\begin{cases} a(\mathbf{v}_h, \mathbf{u}_h) + b(\mathbf{v}_h, p_h) = f(\mathbf{v}_h) & \forall \mathbf{v}_h \in V_h \\ b(\mathbf{u}_h, q_h) + c(q_h, p_h) = 0 & \forall q_h \in Q_h \end{cases} \quad (14)$$

<sup>164</sup> where the spaces  $V_h \subseteq V$ ,  $Q_h \subseteq Q$  are defined by:

$$V_h = \{\mathbf{v}_h \in (\text{span}\{N_I\}_{I=1}^{n_u})^{n_d} | \mathbf{v}_h = \mathbf{g}, \text{ on } \Gamma_g\} \quad (15)$$

$$Q_h = \{q_h \in \text{span}\{\Psi_K\}_{K=1}^{n_p} | \int_{\Omega} q_h d\Omega = 0\} \quad (16)$$

<sup>165</sup> For nearly incompressible material, the Poisson ratio approaches 0.5, and  
<sup>166</sup> the bulk modulus  $\kappa$  will tend to infinity based on Eq. (5). Then, the bilinear  
<sup>167</sup> form  $c$  in Eq. (11) tends to zero. And the weak form of Eq. (14) becomes an  
<sup>168</sup> enforcement of the volumetric strain  $\nabla \cdot \mathbf{u}_h$  to be zero using the Lagrangian  
<sup>169</sup> multiplier method, where  $p_h$  is the Lagrangian multiplier.

<sup>170</sup> Furthermore, from the second line of Eq. (14), we have:

$$b(\mathbf{u}_h, q_h) + c(q_h, p_h) = (q_h, \nabla \cdot \mathbf{u}_h) - (q_h, \frac{1}{3\kappa} p_h) = 0, \quad \forall q_h \in Q_h \quad (17)$$

<sup>171</sup> or

$$(q_h, 3\kappa \nabla \cdot \mathbf{u}_h - p_h) = 0, \quad \forall q_h \in Q_h \quad (18)$$

<sup>172</sup> where  $(\bullet, \bullet)$  is the inner product operator evaluated by:

$$(q, p) := \int_{\Omega} q p d\Omega \quad (19)$$

<sup>173</sup> Obviously, in Eq. (18),  $p_h$  is the orthogonal projection of  $3\kappa\nabla \cdot \mathbf{u}_h$  with respect  
<sup>174</sup> to the space  $Q_h$  [1], and, for further development, we use the nabla notation  
<sup>175</sup> with an upper tilde to denote the projection operator, i.e.,  $p_h = \tilde{\nabla} \cdot \mathbf{u}_h$ . In this  
<sup>176</sup> circumstance, the bilinear form  $b$  in the first line of Eq. (14) becomes:

$$\begin{aligned} b(\mathbf{v}_h, p_h) &= (\underbrace{\nabla \cdot \mathbf{v}_h - \tilde{\nabla} \cdot \mathbf{v}_h, p_h}_{0}) + (\tilde{\nabla} \cdot \mathbf{v}_h, \underbrace{p_h}_{3\kappa\tilde{\nabla} \cdot \mathbf{u}_h}) \\ &= (\tilde{\nabla} \cdot \mathbf{v}_h, 3\kappa\tilde{\nabla} \cdot \mathbf{u}_h) \\ &= \tilde{a}(\mathbf{v}_h, \mathbf{u}_h) \end{aligned} \quad (20)$$

<sup>177</sup> where the bilinear form  $\tilde{a} : V_h \times V_h \rightarrow \mathbb{R}$  is defined by:

$$\tilde{a}(\mathbf{v}_h, \mathbf{u}_h) = \int_{\Omega} 3\kappa\tilde{\nabla} \cdot \mathbf{v}_h \tilde{\nabla} \cdot \mathbf{u}_h d\Omega \quad (21)$$

<sup>178</sup> Accordingly, the problem of Eq. (14) becomes a one-variable form: Find  
<sup>179</sup>  $\mathbf{u}_h \in V_h$ , such that

$$a(\mathbf{v}_h, \mathbf{u}_h) + \tilde{a}(\mathbf{v}_h, \mathbf{u}_h) = f(\mathbf{v}_h), \quad \forall \mathbf{v}_h \in V_h \quad (22)$$

<sup>180</sup> As  $\kappa \rightarrow \infty$ , Eq. (22) can be regarded as an enforcement of volumetric strain  
<sup>181</sup> using the penalty method, where  $\tilde{a}$  is the penalty term. However, it should  
<sup>182</sup> be noted that, if the mixed-formulation wants to obtain a satisfactory result,  
<sup>183</sup> this orthogonal projection must be surjective [57]. In the case where it is not  
<sup>184</sup> surjective, for a given  $p_h \in Q_h$ , it may not be possible to find a  $\mathbf{u}_h \in V_h$  such that  
<sup>185</sup>  $p_h = 3\kappa\tilde{\nabla} \cdot \mathbf{u}_h$ . This will lead to a much smaller displacement than expected and  
<sup>186</sup> an oscillated pressure result. This phenomenon is called volumetric locking.

### <sup>187</sup> 3. Mixed FE–meshfree formulation with optimal constraint ratio

<sup>188</sup> In the proposed mixed-formulation, the displacement is approximated using  
<sup>189</sup> 3-node (Tri3), 6-node (Tri6) triangular elements and 4-node (Quad4), 8-node  
<sup>190</sup> (Quad8) quadrilateral elements in 2D, 4-node (Tet4) tetrahedral element and  
<sup>191</sup> 8-node (Hex8) hexahedral element in 3D [2]. In order to flexibly adjust to let  
<sup>192</sup> the DOFs of pressure meet the optimal constraint, the reproducing kernel (RK)  
<sup>193</sup> meshfree approximation is involved to approximate pressure, namely “FE”-RK  
<sup>194</sup> formulation.

#### <sup>195</sup> 3.1. Reproducing kernel meshfree approximation

<sup>196</sup> In accordance with the reproducing kernel approximation, the entire domain  
<sup>197</sup>  $\Omega$ , as shown in Figure 1, is discretized by  $n_p$  meshfree nodes,  $\{\mathbf{x}_I\}_{I=1}^{n_p}$ . The

<sup>198</sup> approximated pressure, namely  $p_h$ , can be expressed by the shape function  $\Psi_I$   
<sup>199</sup> and nodal coefficient  $p_I$ , yields:

$$p_h(\mathbf{x}) = \sum_{I=1}^{n_p} \Psi_I(\mathbf{x}) p_I \quad (23)$$

<sup>200</sup> where, in the reproducing kernel approximation framework, the shape function  
<sup>201</sup>  $\Psi_I$  is given by:

$$\Psi_I(\mathbf{x}) = \mathbf{c}(\mathbf{x}_I - \mathbf{x}) \mathbf{p}(\mathbf{x}_I - \mathbf{x}) \phi(\mathbf{x}_I - \mathbf{x}) \quad (24)$$

<sup>202</sup> in which  $\mathbf{p}$  is the basis vector, for instance in the context of the 3D quadratic  
<sup>203</sup> case, the basis vector takes the following form:

$$\mathbf{p}(\mathbf{x}) = \{1, x, y, z, x^2, y^2, z^2, xy, xz, yz\}^T \quad (25)$$

<sup>204</sup> and  $\phi$  stands for the kernel function. In this work, the traditional Cubic B-spline  
<sup>205</sup> function with square or cube support is used as the kernel function:

$$\phi(\mathbf{x}_I - \mathbf{x}) = \phi(s_x) \phi(s_y) \phi(s_z), \quad s_i = \frac{\|\mathbf{x}_I - \mathbf{x}\|}{\bar{s}_{iI}} \quad (26)$$

<sup>206</sup> with

$$\phi(s) = \frac{1}{3!} \begin{cases} (2-2s)^3 - 4(1-2s)^3 & s \leq \frac{1}{2} \\ (2-2s)^3 & \frac{1}{2} < s < 1 \\ 0 & s > 1 \end{cases} \quad (27)$$

<sup>207</sup> where  $\bar{s}_{iI}$ 's are the support size towards the  $i$ -direction for the shape function  
<sup>208</sup>  $\Psi_I$ . The correction function  $\mathbf{c}$  can be determined by the following so-called  
<sup>209</sup> consistency condition:

$$\sum_{I=1}^{n_p} \Psi_I(\mathbf{x}) \mathbf{p}(\mathbf{x}_I) = \mathbf{p}(\mathbf{x}) \quad (28)$$

<sup>210</sup> or equivalent shifted form:

$$\sum_{I=1}^{n_p} \Psi_I(\mathbf{x}) \mathbf{p}(\mathbf{x}_I - \mathbf{x}) = \mathbf{p}(\mathbf{0}) \quad (29)$$

<sup>211</sup> The consistency condition ensures that the reproducing kernel shape functions  
<sup>212</sup> are able to reproduce the polynomial space spanned by the basis function  $\mathbf{p}$ ,  
<sup>213</sup> which is a fundamental requirement for the accuracy of the Galerkin method.  
<sup>214</sup> Herein, the order of the basis function  $\mathbf{p}$  is chosen to be the same as the order  
<sup>215</sup> of the displacement approximation.

<sup>216</sup> Further, substituting Eq. 24 into Eq. (29) leads to:

$$\mathbf{c}(\mathbf{x}_I - \mathbf{x}) = \mathbf{A}^{-1}(\mathbf{x}_I - \mathbf{x}) \mathbf{p}(\mathbf{0}) \quad (30)$$

<sup>217</sup> in which  $\mathbf{A}$  is namely the moment matrix evaluated by:

$$\mathbf{A}(\mathbf{x}_I - \mathbf{x}) = \sum_{I=1}^{n_p} \mathbf{p}(\mathbf{x}_I - \mathbf{x}) \mathbf{p}^T(\mathbf{x}_I - \mathbf{x}) \phi(\mathbf{x}_I - \mathbf{x}) \quad (31)$$

<sup>218</sup> Taking Eq. (30) back to Eq. (24), the final form of the reproducing kernel shape  
<sup>219</sup> function can be obtained as:

$$\Psi_I(\mathbf{x}) = \mathbf{p}^T(\mathbf{0})\mathbf{A}^{-1}(\mathbf{x}_I - \mathbf{x})\phi(\mathbf{x}_I - \mathbf{x}) \quad (32)$$

<sup>220</sup> As shown in Figure 1, reproducing kernel meshfree shape functions are glob-  
<sup>221</sup> ally smooth across the entire domain, using them to discretize the pressure field  
<sup>222</sup> allows the constraint ratio to be adjusted arbitrarily, without being limited by  
<sup>223</sup> element topology. Meshfree shape functions generally lack the Kronecker delta  
<sup>224</sup> property, which prevents the direct imposition of essential boundary conditions.  
<sup>225</sup> Fortunately, the mixed formulation shown in Eq. 14 only concerns the displace-  
<sup>226</sup>ment essential boundary condition, and this condition can be easily imposed by  
<sup>227</sup> the standard methods, such as the penalty method that used in this work.

<sup>228</sup> Moreover, when combined with finite element approximations in Eq. 14,  
<sup>229</sup> numerical integration can be conveniently performed within each finite element  
<sup>230</sup> ( $\Omega_C$ 's). The numerical integration issue caused by the loss of variational con-  
<sup>231</sup>sistency between meshfree shape functions and their derivatives [58] would not  
<sup>232</sup> appear in the mixed formulation of Eq. 14, this is due to the fact that Eq.  
<sup>233</sup> 14 solely depends on the meshfree shape functions themselves. Therefore, the  
<sup>234</sup> proposed method employs standard lower-order Gaussian quadrature rules, as  
<sup>235</sup> commonly used in traditional finite element methods, while still maintaining its  
<sup>236</sup> accuracy. Table 1 lists the integration schemes used in this work for mixed-  
<sup>237</sup> formulations. Methods with linear basis functions use an integration scheme of  
<sup>238</sup> order 2. Those with quadratic basis functions use a scheme of order 4. The  
<sup>239</sup> detailed locations and weights of the Gauss points can be found in Ref. [4].

Table 1: Integration schemes for the mixed FE–meshfree formulation

Methods	$n_o$	$n_g$ for $\Omega$	$n_g$ for $\Gamma$
Tri3-RK	2	3	2
Tri6-RK	4	6	3
Quad4-RK	2	$2 \times 2$	2
Quad8-RK	4	$3 \times 3$	3
Tet4-RK	2	4	3
Hex8-RK	2	$2 \times 2 \times 2$	4

$n_o$ : Integration Order     $n_g$ : Number of integration points

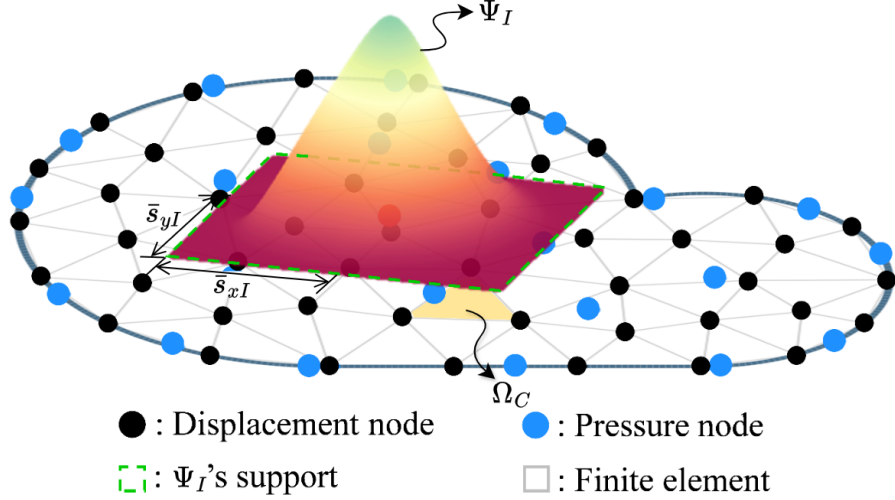


Figure 1: Illustration for reproducing kernel meshfree approximation

240    *3.2. Pressure node distributions with optimal constraint ratio*

241    In this subsection, 2D and 3D inf-sup tests [6], as defined in Eq. ??, are  
242    conducted using the mixed FE-meshfree formulations to validate the proposed  
243    inf-sup value estimator. The 2D test considers the square domain  $\Omega = (0, 1) \times$   
244     $(0, 1)$ , where the displacement is discretized by Tri3 and Quad4 with  $4 \times 4$ ,  
245     $8 \times 8$ ,  $16 \times 16$  and  $32 \times 32$  elements, Tri6 and Quad8 with  $2 \times 2$ ,  $4 \times 4$ ,  $8 \times 8$   
246    and  $16 \times 16$  elements, respectively. The 3D test employs a cube domain  $\Omega =$   
247     $(0, 1) \times (0, 1) \times (0, 1)$  with  $4 \times 4$ ,  $8 \times 8$  and  $16 \times 16$  elements for the Tet4 and Hex8.  
248    For pressure discretization, linear meshfree approximation with a normalized  
249    support size of 1.5 is employed for Tri3, Quad4, Tet4 and Hex8. For Tri6 and  
250    Quad8, a quadratic meshfree approximation with a normalized support size of  
251    2.5 is utilized. In order to avoid the influence of interpolation error, uniform  
252    nodal distributions are used for pressure discretizations, for example in Figure  
253    2, which displays  $4 \times 4$  Quad4 elements with  $4 \times 3$  uniformly distributed pressure  
254    nodes.

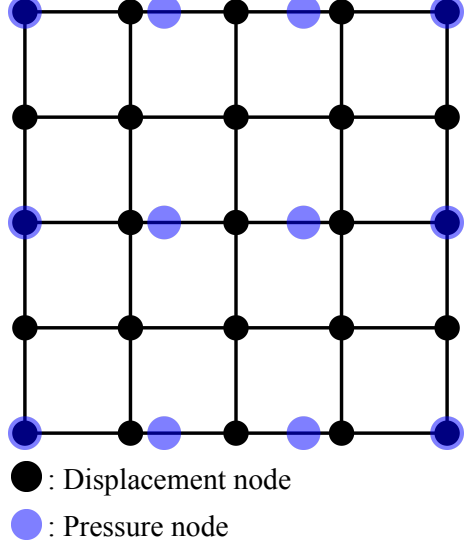


Figure 2: Illustration of uniform nodal distribution for inf-sup test with  $n_u = 5 \times 5$ ,  $n_p = 4 \times 3$

Figures 3–8 show the corresponding results, in which the red line stands for the value of  $\beta$  with respect to the number of pressure nodes  $n_p$ , and the vertical dashed line denotes the stabilized number  $n_s$ . The deeper color of the lines means mesh refinement. The results show that, no matter linear or quadratic elements, as  $n_p$  increases over  $n_s$ , the value of  $\beta$  sharply decreases, and then the inf-sup condition cannot be maintained. This result is consistent with the discussion in Section ??, and again verifies the effect of the proposed estimator.

Moreover, the mixed formulation's results with the traditional optimal constraint ratio  $r = n_d$  are listed in these figures as well, and  $\beta$  in this circumstance is already much smaller than those in the optimal range. Considering the results shown above, the easy programming and efficiency, the pressure nodes are chosen among the displacement nodes. The optimal schemes for linear and quadratic, 2D and 3D element discretizations, namely with  $r = r_{opt}$ , are shown in Figure 9, where every other displacement node is selected as the pressure node. For practical implementations of linear cases, the pressure nodes are initially generated using traditional approaches, such as Delaunay triangulation. Subsequently, the displacement nodes are then obtained through a standard mesh refinement process to the pressure nodes. For quadratic approximations in Tri6 and Quad8 elements, the element vertices are chosen as pressure nodes after displacement element generation. Consequently, all constraint ratios evaluated using the discretizations in Figure 9 fall within the optimal range. The corresponding inf-sup test results for these schemes are also marked in inf-sup test figure and show that, with mesh refinement, their  $\beta$ 's are always maintained at a non-negligible level.

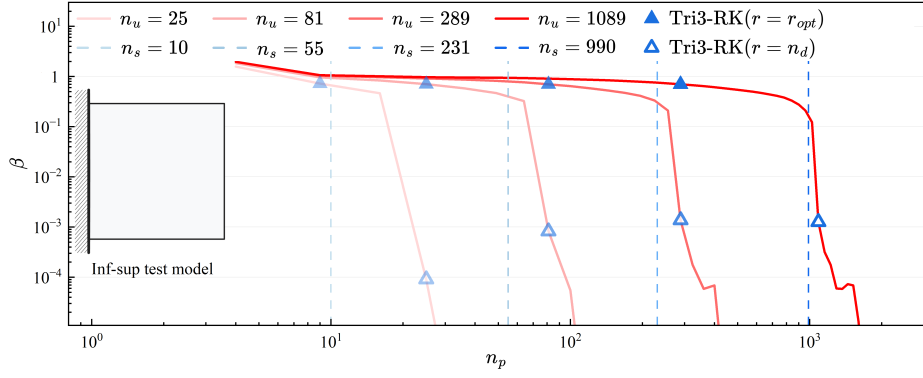


Figure 3: Inf-sup test for Tri3-RK

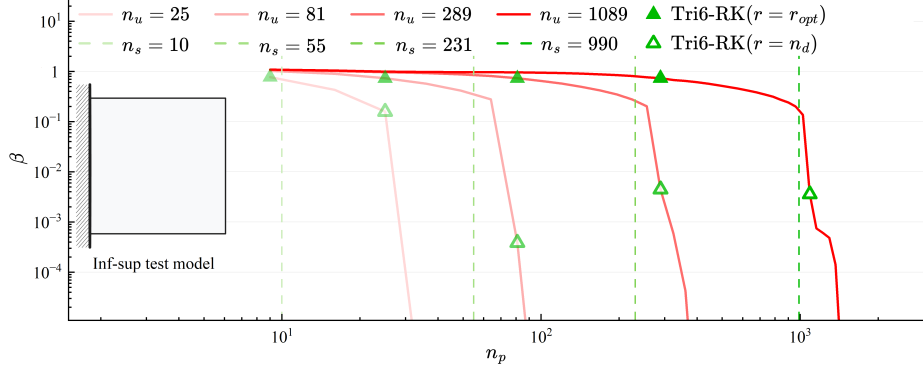


Figure 4: Inf-sup test for Tri6-RK

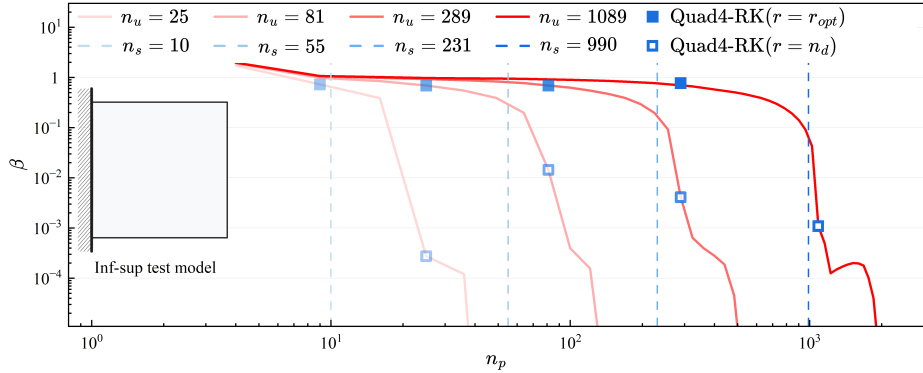


Figure 5: Inf-sup test for Quad4-RK

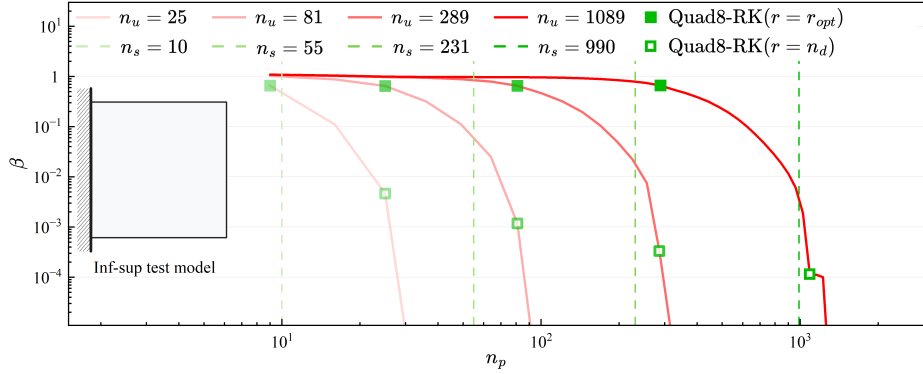


Figure 6: Inf-sup test for Quad8-RK

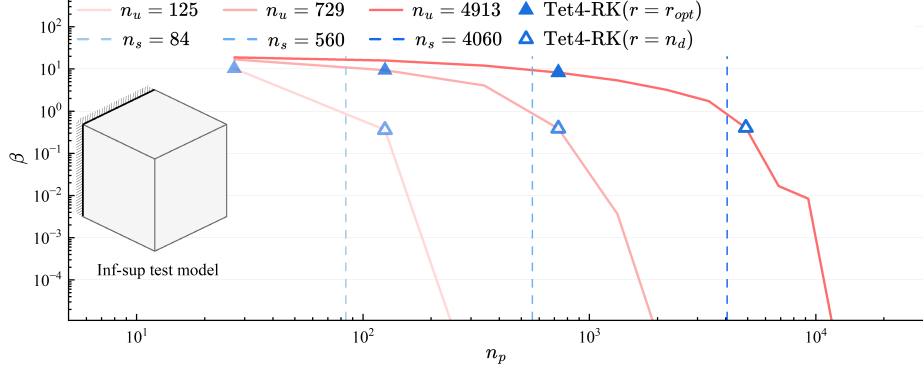


Figure 7: Inf-sup test for Tet4-RK

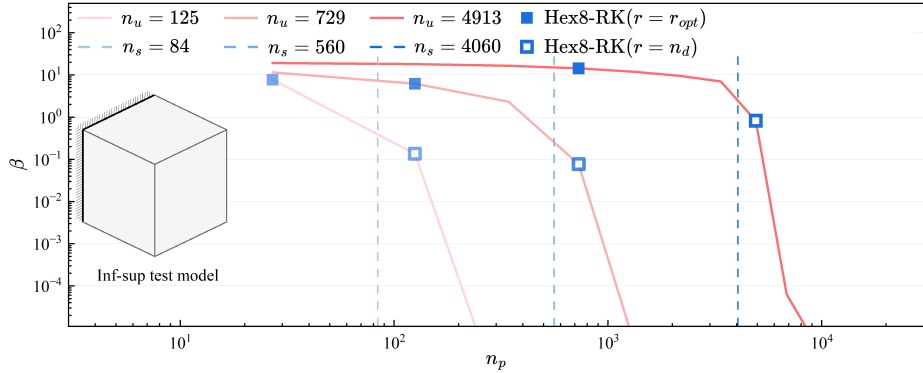


Figure 8: Inf-sup test for Hex8-RK

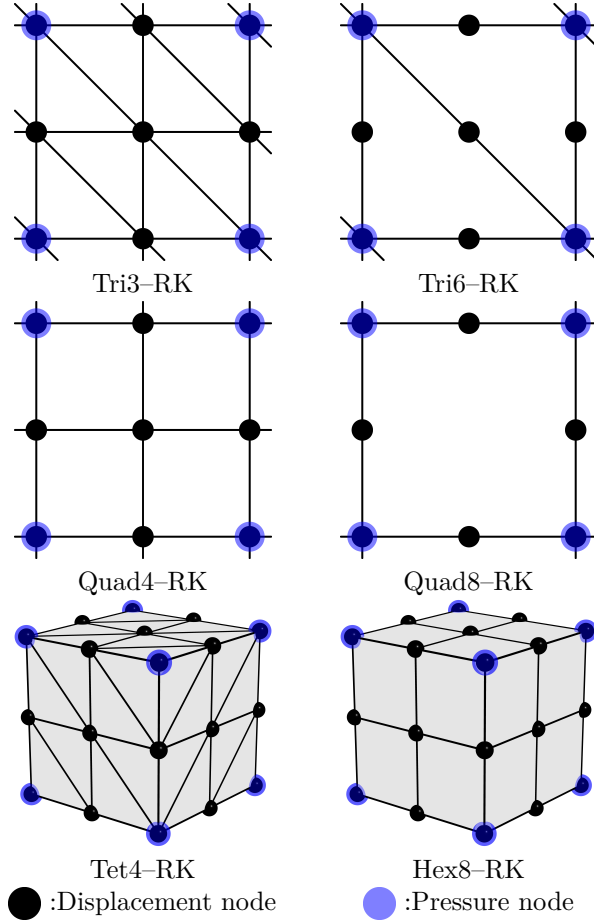


Figure 9: Nodal distribution schemes for mixed FE-meshfree formulations with  $r = r_{opt}$

279    **4. Numerical examples**

280    **4.1. Plate with hole problem**

281    Consider an infinite plate with a hole centered at the origin, as shown in  
 282    Figure 10, and at the infinity towards the  $x$ -direction subjected to a uniform  
 283    traction  $T = 1000$ . The geometric and material parameters for this problem are  
 284    that the ratio of the hole  $a = 1$ , Young's modulus  $E = 3 \times 10^6$ , and Poisson's  
 285    ratio  $\nu = 0.5 - 10^{-8}$ . The analytical solution of this problem refers to the

<sup>286</sup> Michell solution [59] as:

$$\begin{cases} u_x(\rho, \theta) = \frac{Ta}{8\mu} \left( \frac{\rho}{a}(k+1) \cos \theta - \frac{2a^3}{\rho^3} \cos 3\theta + \frac{2a}{\rho} ((1+k) \cos \theta + \cos 3\theta) \right) \\ u_y(\rho, \theta) = \frac{Ta}{8\mu} \left( \frac{\rho}{a}(k-3) \sin \theta - \frac{2a^3}{\rho^3} \sin 3\theta + \frac{2a}{\rho} ((1-k) \sin \theta + \sin 3\theta) \right) \end{cases} \quad (33)$$

<sup>287</sup> in which  $k = \frac{3-\nu}{1+\nu}$ ,  $\mu = \frac{E}{2(1+\nu)}$ . And the stress components are given by:

$$\begin{cases} \sigma_{xx} = T \left( 1 - \frac{a^2}{\rho^2} \left( \frac{3}{2} \cos 2\theta + \cos 4\theta \right) + \frac{3a^4}{2\rho^4} \cos 4\theta \right) \\ \sigma_{yy} = -T \left( \frac{a^2}{\rho^2} \left( \frac{1}{2} \cos 2\theta - \cos 4\theta \right) + \frac{3a^4}{2\rho^4} \cos 4\theta \right) \\ \sigma_{xy} = -T \left( \frac{a^2}{\rho^2} \left( \frac{1}{2} \sin 2\theta + \sin 4\theta \right) - \frac{3a^4}{2\rho^4} \sin 4\theta \right) \end{cases} \quad (34)$$

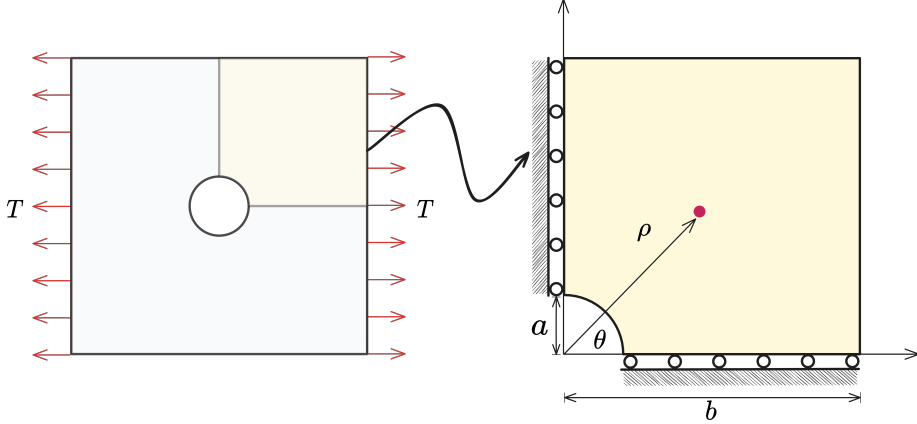


Figure 10: Illustration of plate with hole problem

<sup>288</sup> According to the symmetry property of this problem, only a quarter model  
<sup>289</sup> with length  $b = 5$  is considered as shown in Figure 10. The displacement is  
<sup>290</sup> discretized by 3-node and 6-node triangular elements with 81, 299, 1089, and  
<sup>291</sup> 4225 nodes. The corresponding linear and quadratic meshfree formulations are  
<sup>292</sup> employed for pressure discretization, and the characterized support sizes are  
<sup>293</sup> chosen as 1.5 and 2.5, respectively. Figure 11 studies the relationship between  
<sup>294</sup> strain, pressure errors, and  $n_p$  using the nodal distributions uniformly related  
<sup>295</sup> to displacement nodes. Unlike the quadrilateral element case in Section ??,  
<sup>296</sup> the quadratic Tri6-RK shows worse results while the constraint ratio is out of  
<sup>297</sup> the optimal range. And Tri3-RK exhibits less sensitivity in strain error than  
<sup>298</sup> Tri6-RK, but its error is increasing while  $n_p$  goes up. Both Tri3-RK and Tri6-  
<sup>299</sup> RK with constraint ratios under the optimal range perform acceptably. The  
<sup>300</sup> corresponding error convergence study is presented in Figure 13, the traditional

<sup>301</sup> MINI element and the 6-node triangular displacement element with 3-node  
<sup>302</sup> continuous triangular pressure element (T6C3) are employed for comparison.  
<sup>303</sup> The results show that only Tri3-RK with  $r = 2$  shows a comparable result with  
<sup>304</sup> the optimal one with  $r = r_{opt}$ . The other formulations with the traditional  
<sup>305</sup> constraint ratio show lower accuracy and error convergence rates.

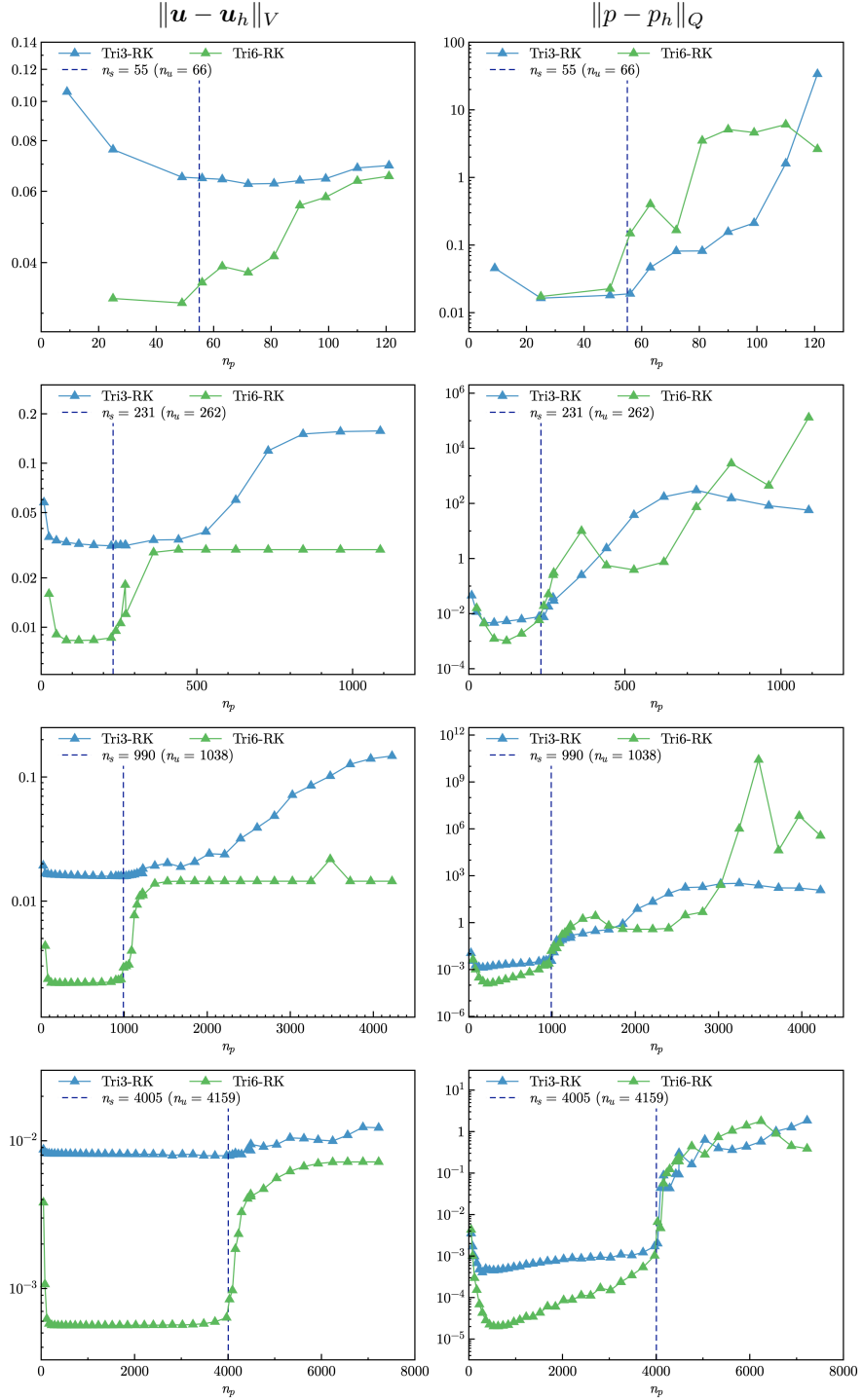


Figure 11: Strain and pressure errors vs.  $n_p$  for plate with hole problem

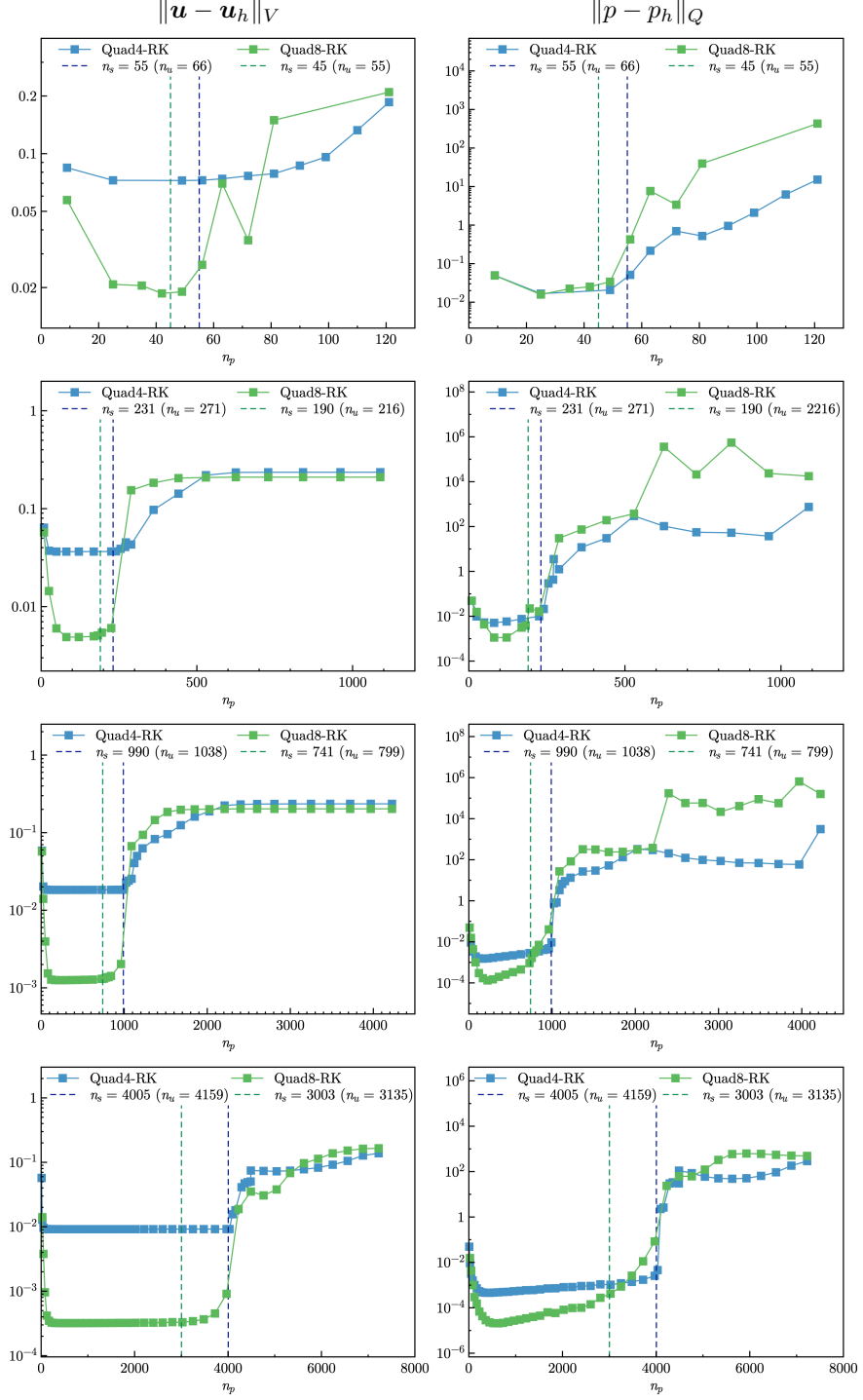


Figure 12: Strain and pressure errors vs.  $n_p$  for plate with hole problem

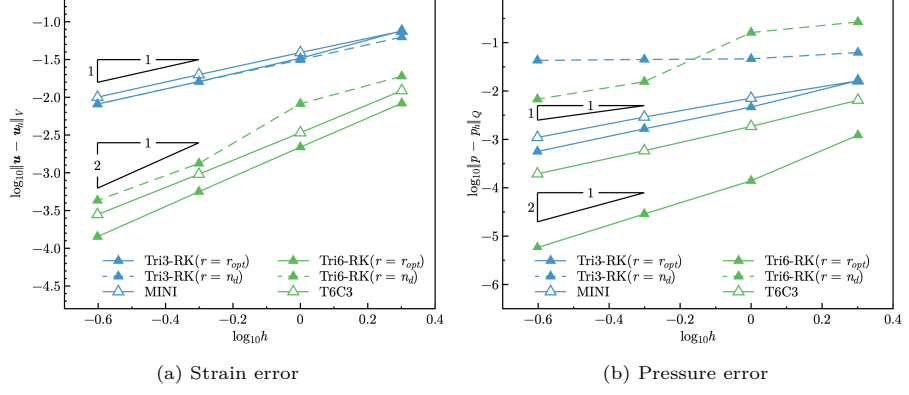


Figure 13: Error convergence study for plate with a hole problem

Furthermore, the influence of the integration scheme for this problem is investigated, as shown in Tables 2 and 3, where the integration order  $n_o$  is varied from 1 to 5 for triangular elements and from 1 to 11 for quadrilateral elements. The results show that the proposed mixed formulations are not sensitive to the integration order, using the traditional lower order Gauss integration scheme can sufficiently obtain accurate results, and it is consistent with the previous analysis in Section 3.1.

Table 2: Error comparison with different triangular integration schemes for plate with a hole problem

$n_o$	$n_g$ for $\Omega$	$n_g$ for $\Gamma$	Tri3-RK		Tri6-RK	
			$\ \mathbf{u} - \mathbf{u}_h\ _V$	$\ p - p_h\ _Q$	$\ \mathbf{u} - \mathbf{u}_h\ _V$	$\ p - p_h\ _Q$
1	1	1	3.11E-2	3.53E-3	8.53E17	1.31E4
2	3	2	3.11E-2	3.67E-3	8.33E-3	1.20E-3
3	4	2	3.11E-2	3.67E-3	8.32E-3	1.20E-3
4	6	3	3.11E-2	3.68E-3	8.32E-3	1.22E-3
5	7	3	3.11E-2	3.68E-3	8.32E-3	1.22E-3

Table 3: Error comparison with different quadrilateral integration schemes for plate with a hole problem

$n_o$	$n_g$ for $\Omega$	$n_g$ for $\Gamma$	Quad4-RK		Quad8-RK	
			$\ \mathbf{u} - \mathbf{u}_h\ _V$	$\ p - p_h\ _Q$	$\ \mathbf{u} - \mathbf{u}_h\ _V$	$\ p - p_h\ _Q$
1	3	1	3.64E-2	5.01E-3	9.53E13	8.15E-1
3	$2 \times 2$	2	3.64E-2	5.09E-3	4.33E-2	8.84E-3
5	$3 \times 3$	3	3.62E-2	3.71E-3	1.27E-3	4.42E-5
7	$4 \times 4$	4	3.62E-2	3.70E-3	1.26E-3	1.49E-4
9	$5 \times 5$	5	3.62E-2	3.70E-3	1.26E-3	1.50E-4
11	$6 \times 6$	6	3.62E-2	3.70E-3	1.26E-3	1.50E-4

$n_o$ : Integration Order     $n_g$ : Number of integration points

### 313 Acknowledgment

314 The support of this work by the National Natural Science Foundation of  
 315 China (12102138), the Natural Science Foundation of Fujian Province of China  
 316 (2023J01108) and the Fundamental Research Funds of Central Universities  
 317 (ZQN-1014) is gratefully acknowledged.

### 318 References

- 319 [1] F. Brezzi, M. Fortin, Mixed and Hybrid Finite Element Methods, Vol. 15 of  
 320 Springer Series in Computational Mathematics, Springer, New York, NY,  
 321 1991.
- 322 [2] T. J. Hughes, The Finite Element Method: Linear Static and Dynamic  
 323 Finite Element Analysis, Prentice Hall, New Jersey, 2000.
- 324 [3] I. Babuška, R. Narasimhan, The Babuška-Brezzi condition and the patch  
 325 test: An example, Computer Methods in Applied Mechanics and Engineering 140 (1-2) (1997) 183–199.
- 327 [4] K. J. Bathe, Finite Element Procedures, Prentice Hall, Englewood Cliffs,  
 328 New Jersey, 1996.
- 329 [5] D. S. Malkus, Eigenproblems associated with the discrete LBB condition for  
 330 incompressible finite elements, International Journal of Engineering Science 19 (10) (1981) 1299–1310.
- 332 [6] D. Chapelle, K. J. Bathe, The inf-sup test, Computers & Structures 47 (4)  
 333 (1993) 537–545.
- 334 [7] F. Brezzi, K. J. Bathe, Studies of finite element procedures the inf-sup  
 335 condition equivalent forms and applications.
- 336 [8] D. Gallistl, Rayleigh–Ritz approximation of the inf-sup constant for the  
 337 divergence, Mathematics of Computation 88 (315) (2019) 73–89.

- 338 [9] P. Hood, C. Taylor, Navier-Stokes equations using mixed interpolation,  
 339 Finite element methods in flow problems (1974) 121–132.
- 340 [10] D. S. Malkus, T. J. Hughes, Mixed finite element methods - Reduced and  
 341 selective integration techniques: A unification of concepts, Computer Meth-  
 342 ods in Applied Mechanics and Engineering 15 (1) (1978) 63–81.
- 343 [11] T. Shilt, R. Deshmukh, J. J. McNamara, P. J. O'Hara, Solution of nearly  
 344 incompressible field problems using a generalized finite element approach,  
 345 Computer Methods in Applied Mechanics and Engineering 368 (2020)  
 346 113165.
- 347 [12] J. C. Simo, M. S. Rifai, A class of mixed assumed strain methods and  
 348 the method of incompatible modes, International Journal for Numerical  
 349 Methods in Engineering 29 (8) (1990) 1595–1638.
- 350 [13] M. Broccardo, M. Micheloni, P. Krysl, Assumed-deformation gradient finite  
 351 elements with nodal integration for nearly incompressible large deformation  
 352 analysis, International Journal for Numerical Methods in Engineering 78 (9)  
 353 (2009) 1113–1134.
- 354 [14] W. M. Coombs, T. J. Charlton, M. Cortis, C. E. Augarde, Overcoming vol-  
 355 umetric locking in material point methods, Computer Methods in Applied  
 356 Mechanics and Engineering 333 (2018) 1–21.
- 357 [15] S. Saloustros, M. Cervera, S. Kim, M. Chiumenti, Accurate and locking-free  
 358 analysis of beams, plates and shells using solid elements, Computational  
 359 Mechanics 67 (2021) 883–914.
- 360 [16] J. Simo, R. Taylor, K. Pister, Variational and projection methods for the  
 361 volume constraint in finite deformation elasto-plasticity, Computer Meth-  
 362 ods in Applied Mechanics and Engineering 51 (1-3) (1985) 177–208.
- 363 [17] C. R. Dohrmann, P. B. Bochev, A stabilized finite element method for the  
 364 Stokes problem based on polynomial pressure projections, International  
 365 Journal for Numerical Methods in Fluids 46 (2) (2004) 183–201.
- 366 [18] A. Valverde-González, J. Reinoso, B. Dorddivanlioglu, M. Paggi, Locking  
 367 treatment of penalty-based gradient-enhanced damage formulation for fail-  
 368 ure of compressible and nearly incompressible hyperelastic materials, Com-  
 369 putational Mechanics 72 (2023) 635–662.
- 370 [19] B.-B. Xu, F. Peng, P. Wriggers, Stabilization-free virtual element method  
 371 for finite strain applications, Computer Methods in Applied Mechanics and  
 372 Engineering 417 (2023) 116555.
- 373 [20] F. S. Liguori, A. Madeo, S. Marfia, G. Garcea, E. Sacco, A stabilization-  
 374 free hybrid virtual element formulation for the accurate analysis of 2D  
 375 elasto-plastic problems, Computer Methods in Applied Mechanics and En-  
 376 gineering 431 (2024) 117281.

- 377 [21] R. Alves de Sousa, R. Natal Jorge, R. Fontes Valente, J. César de Sá, A new  
 378 volumetric and shear locking-free 3D enhanced strain element, *Engineering*  
 379 *Computations* 20 (7) (2003) 896–925.
- 380 [22] K.-J. Bathe, The inf–sup condition and its evaluation for mixed finite ele-  
 381 ment methods, *Computers & Structures* 79 (2) (2001) 243–252.
- 382 [23] T. J. R. Hughes, Multiscale phenomena: Green’s functions, the Dirichlet-  
 383 to-Neumann formulation, subgrid scale models, bubbles and the origins of  
 384 stabilized methods, *Computer Methods in Applied Mechanics and Engi-  
 385 neering* 127 (1) (1995) 387–401.
- 386 [24] R. Rossi, R. Zorrilla, R. Codina, A stabilised displacement-volumetric  
 387 strain formulation for nearly incompressible and anisotropic materials,  
 388 *Computer Methods in Applied Mechanics and Engineering* 377 (2021)  
 389 113701.
- 390 [25] E. Karabelas, M. A. F. Gsell, G. Haase, G. Plank, C. M. Augustin, An  
 391 accurate, robust, and efficient finite element framework with applications to  
 392 anisotropic, nearly and fully incompressible elasticity, *Computer Methods*  
 393 *in Applied Mechanics and Engineering* 394 (2022) 114887.
- 394 [26] R. Codina, I. Castañar, J. Baiges, Finite element approximation of stabi-  
 395 lized mixed models in finite strain hyperelasticity involving displacements  
 396 and stresses and/or pressure—An overview of alternatives, *International*  
 397 *Journal for Numerical Methods in Engineering* (2024) e7540.
- 398 [27] L. Moreno, R. Wuechner, A. Larese, A mixed stabilized MPM formula-  
 399 tion for incompressible hyperelastic materials using Variational Subgrid-  
 400 Scales, *Computer Methods in Applied Mechanics and Engineering* 435  
 401 (2025) 117621.
- 402 [28] T. J. R. Hughes, L. P. Franca, M. Balestra, A new finite element formu-  
 403 lation for computational fluid dynamics: V. Circumventing the babuška-  
 404 brezzi condition: A stable Petrov-Galerkin formulation of the stokes prob-  
 405 lem accommodating equal-order interpolations, *Computer Methods in Ap-  
 406 plied Mechanics and Engineering* 59 (1) (1986) 85–99.
- 407 [29] A. N. Brooks, T. J. R. Hughes, Streamline upwind/Petrov-Galerkin formu-  
 408 lations for convection dominated flows with particular emphasis on the in-  
 409 compressible Navier-Stokes equations, *Computer Methods in Applied Me-  
 410 chanics and Engineering* 32 (1) (1982) 199–259.
- 411 [30] L. He, L. Jing, M. Feng, New stabilized mixed finite element methods for  
 412 two-field poroelasticity with low permeability, *Applied Mathematics and*  
 413 *Computation* 494 (2025) 129285.
- 414 [31] D. N. Arnold, F. Brezzi, M. Fortin, A stable finite element for the Stokes  
 415 equations, *CALCOLO* 21 (4) (1984) 337–344.

- 416 [32] F. Auricchio, L. Beirão da Veiga, C. Lovadina, A. Reali, A stability study of  
 417 some mixed finite elements for large deformation elasticity problems, Computer Methods in Applied Mechanics and Engineering 194 (9-11) (2005)  
 418 1075–1092.
- 420 [33] A. Quarteroni, A. Valli, Numerical Approximation of Partial Differential  
 421 Equations, Springer Series in Computational Mathematics, Springer,  
 422 Berlin, 1994.
- 423 [34] M. Crouzeix, P. Raviart, Conforming and nonconforming finite ele-  
 424 ment methods for solving the stationary Stokes equations I, Revue  
 425 française d'automatique informatique recherche opérationnelle. Mathéma-  
 426 tique 7 (R3) (1973) 33–75.
- 427 [35] U. Brink, E. Stein, On some mixed finite element methods for incompress-  
 428 ible and nearly incompressible finite elasticity, Computational Mechanics  
 429 19 (1) (1996) 105–119.
- 430 [36] T. Belytschko, Y. Y. Lu, L. Gu, Element-free Galerkin methods, Interna-  
 431 tional Journal for Numerical Methods in Engineering 37 (2) (1994) 229–256.
- 432 [37] W. K. Liu, S. Jun, Y. F. Zhang, Reproducing kernel particle methods, In-  
 433 ternational Journal for Numerical Methods in Fluids 20 (8-9) (1995) 1081–  
 434 1106.
- 435 [38] C. Rodriguez, T.-H. Huang, A variationally consistent reproducing ker-  
 436 nel enhanced material point method and its applications to incompressible  
 437 materials, Computational Mechanics (2023) 1–20.
- 438 [39] S. W. Chi, J. S. Chen, H. Y. Hu, A weighted collocation on the strong form  
 439 with mixed radial basis approximations for incompressible linear elasticity,  
 440 Computational Mechanics 53 (2) (2014) 309–324.
- 441 [40] L. Wang, Z. Qian, Y. Zhou, Y. Peng, A weighted meshfree collocation  
 442 method for incompressible flows using radial basis functions, Journal of  
 443 Computational Physics 401 (2020) 108964.
- 444 [41] A. Ortiz-Bernardin, M. Puso, N. Sukumar, Improved robustness for nearly-  
 445 incompressible large deformation meshfree simulations on Delaunay tes-  
 446 sellations, Computer Methods in Applied Mechanics and Engineering 293  
 447 (2015) 348–374.
- 448 [42] T. J. Hughes, J. A. Cottrell, Y. Bazilevs, Isogeometric analysis: CAD,  
 449 finite elements, NURBS, exact geometry and mesh refinement, Computer  
 450 Methods in Applied Mechanics and Engineering 194 (39-41) (2005) 4135–  
 451 4195.
- 452 [43] F. Auricchio, L. Beirão da Veiga, C. Lovadina, A. Reali, The importance  
 453 of the exact satisfaction of the incompressibility constraint in nonlinear  
 454 elasticity: Mixed FEMs versus NURBS-based approximations, Computer  
 455 Methods in Applied Mechanics and Engineering 199 (5) (2010) 314–323.

- 456 [44] A. Huerta, S. Fernández-Méndez, Locking in the incompressible limit for  
 457 the element-free Galerkin method, International Journal for Numerical  
 458 Methods in Engineering 51 (11) (2001) 1361–1383.
- 459 [45] J. Dolbow, T. Belytschko, Volumetric locking in the element free Galerkin  
 460 method, International Journal for Numerical Methods in Engineering 46 (6)  
 461 (1999) 925–942.
- 462 [46] G. Moutsanidis, J. J. Koester, M. R. Tupek, J.-S. Chen, Y. Bazilevs, Treat-  
 463 ment of near-incompressibility in meshfree and immersed-particle methods,  
 464 Computational Particle Mechanics 7 (2) (2020) 309–327.
- 465 [47] G. Moutsanidis, W. Li, Y. Bazilevs, Reduced quadrature for FEM, IGA  
 466 and meshfree methods, Computer Methods in Applied Mechanics and En-  
 467 gineering 373 (2021) 113521.
- 468 [48] Z.-Y. Wang, Y.-F. Jin, Z.-Y. Yin, Y.-Z. Wang, Overcoming volumetric  
 469 locking in stable node-based smoothed particle finite element method with  
 470 cubic bubble function and selective integration, International Journal for  
 471 Numerical Methods in Engineering 123 (24) (2022) 6148–6169.
- 472 [49] T. Elguedj, Y. Bazilevs, V. Calo, T. Hughes, B<sup>−</sup> and F<sup>−</sup> projection meth-  
 473 ods for nearly incompressible linear and non-linear elasticity and plasticity  
 474 using higher-order NURBS elements, Computer Methods in Applied Me-  
 475 chanics and Engineering 197 (33-40) (2008) 2732–2762.
- 476 [50] J. S. Chen, S. Yoon, H. P. Wang, W. K. Liu, An improved reproducing  
 477 kernel particle method for nearly incompressible finite elasticity, Computer  
 478 Methods in Applied Mechanics and Engineering 181 (1) (2000) 117–145.
- 479 [51] C. M. Goh, P. M. F. Nielsen, M. P. Nash, A stabilised mixed mesh-  
 480 free method for incompressible media: Application to linear elasticity and  
 481 Stokes flow, Computer Methods in Applied Mechanics and Engineering 329  
 482 (2018) 575–598.
- 483 [52] D. S. Bombarde, M. Agrawal, S. S. Gautam, A. Nandy, Hellinger–Reissner  
 484 principle based stress–displacement formulation for three-dimensional iso-  
 485 geometric analysis in linear elasticity, Computer Methods in Applied Me-  
 486 chanics and Engineering 394 (2022) 114920.
- 487 [53] H. Casquero, M. Golestanian, Vanquishing volumetric locking in quadratic  
 488 NURBS-based discretizations of nearly-incompressible linear elasticity:  
 489 CAS elements, Computational Mechanics 73 (6) (2024) 1241–1252.
- 490 [54] A. Huerta, Y. Vidal, P. Villon, Pseudo-divergence-free element free  
 491 Galerkin method for incompressible fluid flow, Computer Methods in Ap-  
 492 plied Mechanics and Engineering 193 (12-14) (2004) 1119–1136.

- 493 [55] C. T. Wu, W. Hu, J. S. Chen, A meshfree-enriched finite element method  
494 for compressible and near-incompressible elasticity, International Journal  
495 for Numerical Methods in Engineering 90 (7) (2012) 882–914.
- 496 [56] T. Vu-Huu, C. Le-Thanh, H. Nguyen-Xuan, M. Abdel-Wahab, A high-  
497 order mixed polygonal finite element for incompressible Stokes flow analy-  
498 sis, Computer Methods in Applied Mechanics and Engineering 356 (2019)  
499 175–198.
- 500 [57] E. Stein, R. de Borst, T. J. R. Hughes (Eds.), Encyclopedia of Compu-  
501 tational Mechanics, John Wiley, Chichester, West Sussex, 2004.
- 502 [58] J. Wu, D. Wang, An accuracy analysis of Galerkin meshfree methods ac-  
503 counting for numerical integration, Computer Methods in Applied Mechan-  
504 ics and Engineering 375 (2021) 113631.
- 505 [59] S. Timoshenko, J. Goodier, Theory of Elasticity, Engineering Mechanics  
506 Series, McGraw-Hill, 1969.
- 507 [60] S. C. Brenner, L. R. Scott, The Mathematical Theory of Finite Element  
508 Methods, Springer, New York, 2008.

509    **Appendix A. Error estimator for mixed-formulation**

510    In this appendix, the traditional error estimators for mixed-formulation are  
 511    illustrated herein, the proof is referred to [60]. For incompressible elasticity  
 512    problems, i.e.  $\kappa \rightarrow \infty$ ,  $c(q, p) = 0$ , the weak formula of Eq. (14) is rewritten as:  
 513    Find  $\mathbf{u}_h \in V_h, p_h \in Q_h$ ,

$$\begin{aligned} a(\mathbf{v}_h, \mathbf{u}_h) + b(\mathbf{v}_h, p_h) &= f(\mathbf{v}_h), & \forall \mathbf{v}_h \in V_h \\ b(\mathbf{u}_h, q_h) &= 0, & \forall q_h \in Q_h \end{aligned} \quad (\text{A.1})$$

514    According to the definition of bilinear form  $b$  in Eq. (10), for a  $\mathbf{u}_h \in \ker \mathcal{P}_h$ , then  
 515    the second equation of Eq. (A.1) is naturally satisfied. Thus, the above weak  
 516    formulation can be equivalently split into the following two steps: Firstly, find  
 517     $\mathbf{u}_h \in \ker \mathcal{P}_h$ ,

$$a(\mathbf{v}_h, \mathbf{u}_h) = f(\mathbf{v}_h), \quad \forall \mathbf{v}_h \in \ker \mathcal{P}_h \quad (\text{A.2})$$

518    After determine  $\mathbf{u}_h$ , then find  $p_h \in Q_h$ ,

$$b(\mathbf{v}_h, p_h) = f(\mathbf{v}_h) - a(\mathbf{v}_h, \mathbf{u}_h), \quad \forall \mathbf{v}_h \in V_h \quad (\text{A.3})$$

519    To further analyze the error of mixed-formulation, the following properties  
 520    of bilinear forms  $a$  and  $b$  should be defined [60]:

521    • **Continuity:**

$$a(\mathbf{v}, \mathbf{u}) \leq C_a \|\mathbf{v}\|_V \|\mathbf{u}\|_V, \quad \forall \mathbf{v}, \mathbf{u} \in V \quad (\text{A.4})$$

$$b(\mathbf{v}, q) \leq C_b \|\mathbf{v}\|_V \|q\|_Q, \quad \forall \mathbf{v} \in V, \forall q \in Q \quad (\text{A.5})$$

522    • **Coercivity:**

$$\|\mathbf{v}\|_V \leq \frac{1}{\alpha} \sup_{\mathbf{w} \in V} \frac{|a(\mathbf{v}, \mathbf{w})|}{\|\mathbf{w}\|_V}, \quad \forall \mathbf{v} \in V \quad (\text{A.6})$$

523    • **Inf-sup condition:**

$$\|q\|_Q \leq \frac{1}{\beta} \sup_{\mathbf{v} \in V} \frac{|b(\mathbf{v}, q)|}{\|\mathbf{v}\|_V}, \quad \forall q \in Q \quad (\text{A.7})$$

524    where  $C_a$  and  $C_b$  are positive constants independent of mesh size  $h$ .  $\alpha$  and  $\beta$   
 525    are the coercivity and inf-sup constants, respectively, which will influence the  
 526    accuracy of mixed-formulation.

527    For the error of displacement, the Céa's Theorem used for the error analysis  
 528    of traditional Galerkin formulation is not always valid for mixed-formulation.  
 529    This is because most of mixed-formulation can not ensure  $\ker \mathcal{P}_h \subset \ker \mathcal{P}$  to  
 530    maintain the orthogonality of bilinear form  $a$  that is required in the proof of  
 531    Céa's Theorem. So we first introduce the following error estimator for displacement  
 532    in the case of  $\ker \mathcal{P}_h \not\subset \ker \mathcal{P}$ . For any  $\mathbf{v}_h \in \ker \mathcal{P}_h$ , considering the triangle

533 inequality, the coercivity in Eq. (A.6) and the continuity in Eq. (A.4), we have:

$$\begin{aligned}
\|\mathbf{u} - \mathbf{u}_h\|_V &\leq \|\mathbf{u} - \mathbf{v}_h\|_V + \|\mathbf{v}_h - \mathbf{u}_h\|_V \\
&\leq \|\mathbf{u} - \mathbf{v}_h\|_V + \frac{1}{\alpha} \sup_{\mathbf{w}_h \in \ker \mathcal{P}_h} \frac{|a(\mathbf{v}_h - \mathbf{u}_h, \mathbf{w}_h)|}{\|\mathbf{w}_h\|_V} \\
&\leq \|\mathbf{u} - \mathbf{v}_h\|_V + \frac{1}{\alpha} \sup_{\mathbf{w}_h \in \ker \mathcal{P}_h} \frac{|a(\mathbf{v}_h - \mathbf{u}, \mathbf{w}_h)| + |a(\mathbf{u} - \mathbf{u}_h, \mathbf{w}_h)|}{\|\mathbf{w}_h\|_V} \quad (\text{A.8}) \\
&\leq (1 + \frac{C}{\alpha}) \|\mathbf{u} - \mathbf{v}_h\|_V + \frac{1}{\alpha} \sup_{\mathbf{w}_h \in \ker \mathcal{P}_h} \frac{|a(\mathbf{u} - \mathbf{u}_h, \mathbf{w}_h)|}{\|\mathbf{w}_h\|_V}
\end{aligned}$$

534 According to Eqs. (A.2), (A.3) and continuity in Eq. (A.5), the second term on  
535 the right hand side of above equation can be rewritten as:

$$\begin{aligned}
\sup_{\mathbf{w}_h \in \ker \mathcal{P}_h} \frac{|a(\mathbf{u} - \mathbf{u}_h, \mathbf{w}_h)|}{\|\mathbf{w}_h\|_V} &= \sup_{\mathbf{w}_h \in \ker \mathcal{P}_h} \frac{|a(\mathbf{u}, \mathbf{w}_h) - f(\mathbf{w}_h)|}{\|\mathbf{w}_h\|_V} \\
&= \sup_{\mathbf{w}_h \in \ker \mathcal{P}_h} \frac{|b(\mathbf{w}_h, p)|}{\|\mathbf{w}_h\|_V} \quad (\text{A.9}) \\
&= \sup_{\mathbf{w}_h \in \ker \mathcal{P}_h} \frac{|b(\mathbf{w}_h, p - q_h)|}{\|\mathbf{w}_h\|_V} \\
&\leq C_b \|p - q_h\|_Q
\end{aligned}$$

536 where  $q_h$  is an arbitrary variable in  $Q_h$ . Combining the Eqs. (A.8) and (A.9),  
537 the following error estimator for displacement can be obtained:

$$\|\mathbf{u} - \mathbf{u}_h\|_V \leq (1 + \frac{C_a}{\alpha}) \inf_{\mathbf{v}_h \in \ker \mathcal{P}_h} \|\mathbf{u} - \mathbf{v}_h\|_V + \frac{C_b}{\alpha} \inf_{q_h \in Q_h} \|p - q_h\|_Q \quad (\text{A.10})$$

538 Furthermore, for the error estimator of pressure, according to the first equa-  
539 tion of Eq. (6) and  $V_h \subset V$ , we have:

$$b(\mathbf{v}_h, p) = f(\mathbf{v}_h) - a(\mathbf{v}_h, \mathbf{u}), \quad \forall \mathbf{v}_h \in V_h \quad (\text{A.11})$$

540 and then subtracting Eq. (A.11) from Eq. (A.3) yields:

$$b(\mathbf{v}_h, p - p_h) = -a(\mathbf{v}_h, \mathbf{u} - \mathbf{u}_h), \quad \forall \mathbf{v}_h \in V_h \quad (\text{A.12})$$

541 In this context, for any  $q_h \in Q_h$ , invoking the triangle inequality, Eqs. (A.7)  
542 and (A.5) leads to:

$$\begin{aligned}
\|p - p_h\|_Q &\leq \|p - q_h\|_Q + \|q_h - p_h\|_Q \\
&\leq \|p - q_h\|_Q + \frac{1}{\beta} \sup_{\mathbf{v} \in V_h} \frac{|b(\mathbf{v}_h, q_h - p_h)|}{\|\mathbf{v}_h\|_V} \\
&\leq \|p - q_h\|_Q + \frac{1}{\beta} \sup_{\mathbf{v} \in V_h} \frac{|a(\mathbf{v}_h, \mathbf{u} - \mathbf{u}_h)| + |b(\mathbf{v}_h, p - q_h)|}{\|\mathbf{v}_h\|_V} \quad (\text{A.13}) \\
&\leq \frac{C_a}{\beta} \|\mathbf{u} - \mathbf{u}_h\|_V + (1 + \frac{C_b}{\beta}) \|p - q_h\|_Q
\end{aligned}$$

543 Consequently, the error estimator for pressure can be given by:

$$\|p - p_h\|_Q \leq \frac{C_a}{\beta} \|\mathbf{u} - \mathbf{u}_h\|_V + \left(1 + \frac{C_b}{\beta}\right) \inf_{q_h \in Q_h} \|p - q_h\|_Q \quad (\text{A.14})$$

544 Obviously, the error estimators of Eqs. (A.10) and (A.14) are both related  
 545 to the coercivity constant  $\alpha$ , inf-sup constant  $\beta$  and the approximability of  
 546 spaces  $\ker \mathcal{P}_h$ ,  $Q_h$ , in which the approximability is usually measured by the  
 547 interpolation error of approximation method. However, the approximability  
 548 of space  $\ker \mathcal{P}_h$  is not trivial to be evaluated directly. To further evaluate the  
 549 approximability of space  $\ker \mathcal{P}_h$ , let a variable  $\mathbf{w}_h \in V_h \setminus \ker \mathcal{P}_h$  to satisfy the  
 550 following relationship:

$$\inf_{\bar{\mathbf{v}}_h \in \ker \mathcal{P}_h} \|\mathbf{u} - (\bar{\mathbf{v}}_h + \mathbf{w}_h)\|_V = \inf_{\mathbf{v}_h \in V_h} \|\mathbf{u} - \mathbf{v}_h\|_V \quad (\text{A.15})$$

551 such that the approximability of space  $\ker \mathcal{P}_h$  can be transformed to that of  
 552 space  $V_h$  that is easy to be measured. If  $\mathbf{w}_h = \mathbf{0}$ ,  $\ker \mathcal{P}_h$  has the identical  
 553 approximability with  $V_h$ :

$$\inf_{\bar{\mathbf{v}}_h \in \ker \mathcal{P}_h} \|\mathbf{u} - \bar{\mathbf{v}}_h\|_V = \inf_{\mathbf{v}_h \in V_h} \|\mathbf{u} - \mathbf{v}_h\|_V \quad (\text{A.16})$$

554 If  $\mathbf{w}_h \neq \mathbf{0}$ , leading a triangle inequality we have:

$$\|\mathbf{u} - \bar{\mathbf{v}}_h\|_V \leq \|\mathbf{u} - (\bar{\mathbf{v}}_h + \mathbf{w}_h)\|_V + \|\mathbf{w}_h\|_V \quad (\text{A.17})$$

555 where, reconsidering the Eq. (??) in Lemma ??, as  $\mathbf{w}_h \in V_h \setminus \ker \mathcal{P}_h$  and  
 556  $\mathbf{w}_h \neq \mathbf{0}$ , the following relation can be obtained:

$$\|\mathbf{w}_h\|_V \leq \frac{1}{\beta} \|\mathcal{P}_h \mathbf{w}_h\|_Q \quad (\text{A.18})$$

557 where, using Eqs. (??), (17) and considering  $\mathbf{u} \in \ker \mathcal{P}$ ,  $\bar{\mathbf{v}}_h \in \ker \mathcal{P}_h$ , the right  
 558 hand side of above equation can further be transformed as follows:

$$\begin{aligned} \|\mathcal{P}_h \mathbf{w}_h\|_Q &= \sup_{q_h \in Q_h} \frac{|\frac{1}{\kappa}(\mathcal{P}_h \mathbf{w}_h, q_h)|}{\|q_h\|_Q} = \sup_{q_h \in Q_h} \frac{|b(\mathbf{w}_h, q_h)|}{\|q_h\|_Q} \\ &= \sup_{q_h \in Q_h} \frac{|b(\mathbf{u} - (\mathbf{w}_h + \bar{\mathbf{v}}_h), q_h)|}{\|q_h\|_Q} \\ &\leq C_b \|\mathbf{u} - (\mathbf{w}_h + \bar{\mathbf{v}}_h)\|_V \end{aligned} \quad (\text{A.19})$$

559 With the combination of Eqs. (A.17), (A.18) and (A.19), the approximability  
 560 of  $\ker \mathcal{P}_h$  for the case of  $\mathbf{w}_h \neq \mathbf{0}$  is given by:

$$\inf_{\bar{\mathbf{v}}_h \in \ker \mathcal{P}_h} \|\mathbf{u} - \bar{\mathbf{v}}_h\|_V \leq \left(1 + \frac{C_b}{\beta}\right) \inf_{\mathbf{v}_h \in V_h} \|\mathbf{u} - \mathbf{v}_h\|_V \quad (\text{A.20})$$